Quantum Electronics **49** (3) 266–271 (2019)

https://doi.org/10.1070/QEL16725

Simulation of an electro-optic modulator based on the quantum-confined Stark effect in a two-layer InAlGaAs rib waveguide on an InP substrate

A.V. Tsarev, R.M. Taziev

Abstract. **An electro-optic Mach–Zehnder modulator based on the quantum-confinement Stark effect in layered multiple-quantum-well InAlGaAs structures on InP substrate is numerically simulated. The novelty of the modulator design is the use of a two-layer rib optical waveguides, which provide technologically efficient (loss of 1.5 dB per element) coupling of the modulator with optical fibre. It is shown that, changing the electrode width and the distance between two waveguides in two Mach–Zehnder interferometer arms, one can match the impedance of the modulator with an external 50-Ω load and the velocities of microwave and optical waves in the modulator. The results of the study can be used in integrated optics, optical communication, and radiophotonics devices.**

Keywords: *electro-optic modulator, quantum-confined Stark effect, numerical simulation, integrated optics, radiophotonics.*

1. Introduction

Optical modulators are the main interface elements used to convert an electric signal from an electronic circuit into an optical signal [1, 2]. They are highly demanded for in data transmission and processing systems of fibre optic communication lines between data centres in modern computer systems.

Among many technological platforms used to design ultrabroadband microwave electro-optic modulators, the popular ones are those based on lithium niobate [3, 4] or electro-optic polymers [5, 6] (including hybrid polymer–semiconductor modulators); modulators in silicon-on-insulator (SOI) structures [7, 8], which use free-carrier injection or depletion; and modulators based on the quantum-confinement Stark effect in layered multiple-quantum-well (QW) structures [9, 10], layer-by-layer epitaxially grown on InP substrates. As compared with electro-optic modulators on silicon, lithium niobate, and polymers, the modulators based on quantum-confinement Stark effect can be driven by much lower voltages. At the same time, they are very compact and provide a modulation bandwidth of several tens of gigahertz. A specific feature of such a modulator is that it can easily be integrated with a distributed-feedback laser diode in the form of a monolithic photonic integrated circuit for data generation, processing, and transmission.

In this paper, we report the results of numerical simulation of a new version of an electro-optic modulator based on the quantum-confinement Stark effect in InAlGaAs structures manufactured on an InP substrate. A specific feature of the proposed modulator design (Fig. 1) is that a superlattice of multiple InAlGaAs-based QWs is located above a relatively thick buffer $In_{0.52}Al_{0.48}As$ layer, whose refractive index (3.1973) exceeds that of the adjacent InP substrate (3.1645). Therefore, the formation of a rib waveguide modulator structure provides this design with properties of a double two-layer rib waveguide. The QW-containing layer with a high refractive index is a waveguiding layer, in which the fundamental optical mode with a low cross section (convenient for electro-optic control) is formed. If the waveguide has a smaller width, the optical mode is "pushed out" from the main QW-containing optical waveguide into the $In_{0.52}Al_{0.48}As$ buffer layer, and an increase in the mode field cross section provides convenient coupling with an optical fibre.

2. Simulation of optical waveguide with taking into account the quantum Stark effect

The optical properties of QW-based waveguides are determined to a great extent by the quantum Stark effect, which leads to a strong dependence of the real and imaginary parts of refractive index on the electric field and optical wavelength. The driving electrodes, contacting with heavily doped regions (see Fig. 1), provide a strong electric field, directed normally to the QW layer boundaries. We performed a numerical analysis using the RSoft package [11] with the MultiPhysics Carrier Utility for calculating the refractive index perturbation in a heterostructure modulated by an external electric field. The first step in the calculation is to find the electric potential distribution over the entire layered structure, with the doping level of all layers, after which the quantum-mechanical problem is solved, and the change in the real and imaginary parts of the refractive index is determined with allowance for the electric field effect on the excitons formed in the QW [12–16]. The calculations within the RSoft package show that the optical properties of these structures can be efficiently driven by an external electric field, which changes significantly the real and imaginary parts of the refractive index (Fig. 2). This change leads to strong decay of optical wave. However, for short (~500 μm) QW-based modulator struc-

A.V. Tsarev A.V. Rzhanov Institute of Semiconductor Physics, Siberian Branch, Russian Academy of Sciences, prosp. Akad. Lavrent'eva 13, 630090 Novosibirsk, Russia; Novosibirsk State University, ul. Pirogova 2, 630090 Novosibirsk, Russia; e-mail: tsarev@isp.nsc.ru;
R.M. Taziev A.V. Rzhanov Institute of Semiconductor Physics, Siberian Branch, Russian Academy of Sciences, prosp. Akad. Lavrent'eva 13, 630090 Novosibirsk, Russia; e-mail: taziev@isp.nsc.ru

Received 10 May 2018; revision received 20 July 2018
Kvantovaya Elektronika **49** (3) 266–271 (2019)
Translated by Yu.P. Sin'kov

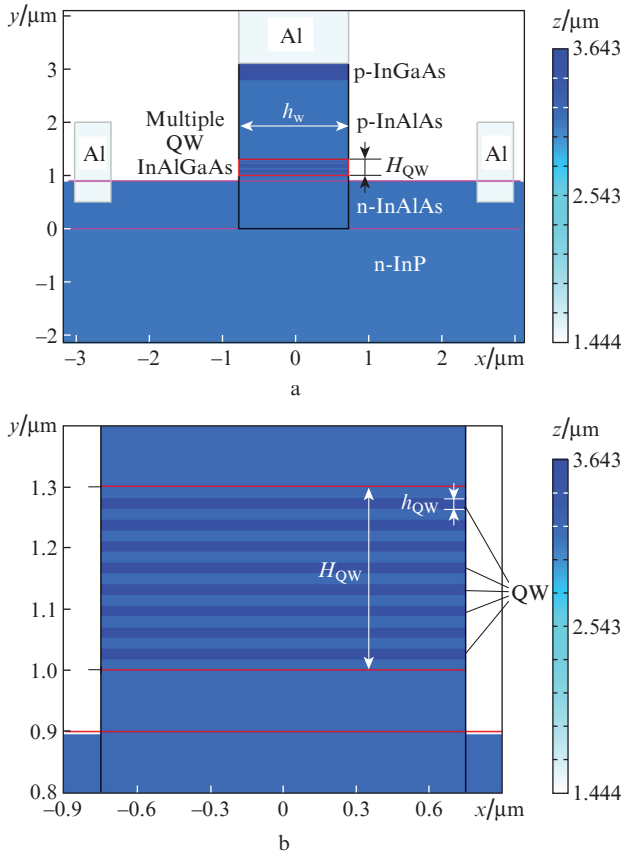

Figure 1. Typical transverse distributions of the refractive index in a modulator with a superlattice of InGaAlAs QWs on an InP substrate: (a) over the entire structure (the maximum corresponds to InGaAs) and (b) in the QW region (the maximum corresponds to the $In_{0.52}Al_{0.09}Ga_{0.38}As$ QW, where the refractive index is higher by 0.18 due to the quantum Stark effect at zero field). Aluminium control electrodes are shown as bright rectangles. The waveguide has a waveguide-layer thickness H_{QW} = 300 nm, it consists of 8 QWs, each of thickness h_{QW} = 16 nm, formed by periodic layers $In_{0.52}Al_{0.09}Ga_{0.38}As$ (QW) and $In_{0.53}Al_{0.3}Ga_{0.17}As$ (buffer) on an InP substrate.

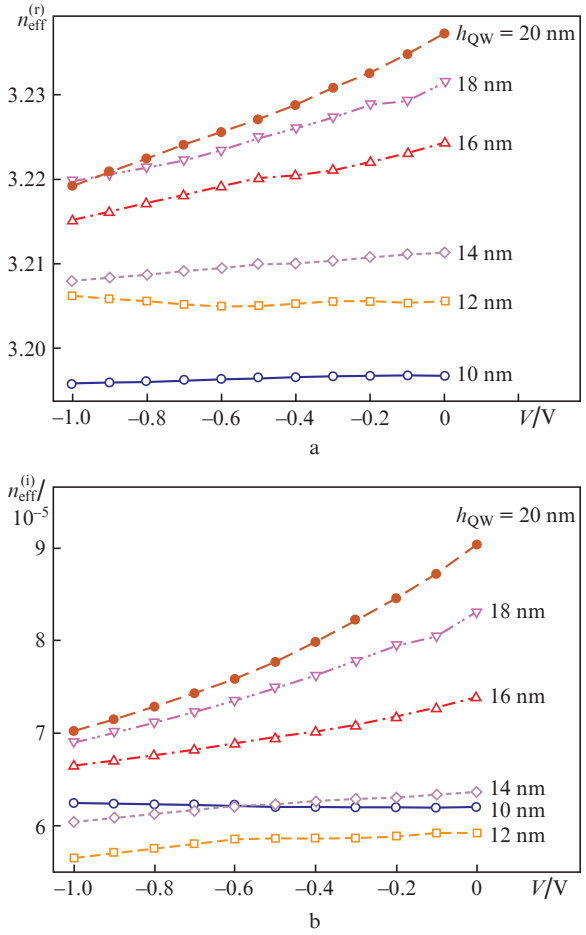

Figure 2. Dependences of the (a) real ($n_{eff}^{(r)}$) and (b) imaginary ($n_{eff}^{(i)}$) parts of the effective refractive index of the fundamental TE mode on the voltage applied across the electrodes for QWs of different thicknesses h_{QW}. The waveguide layer consists of 8 QWs; H_{QW} = 300 nm, the operating wavelength is 1.55 μm.

tures, the total decay is sufficiently small to use them in practice.

To optimise the structures, we calculated the dependence of the effective refractive index (ERI) n_{eff} of the fundamental TE mode on the voltage applied across the electrodes in structures with InAlGaAs QWs of different thicknesses (Fig. 2). Knowing the dependences of the real and imaginary parts of n_{eff} on the modulation voltage, one can calculate the optical wave power transmitted through a Mach–Zehnder interferometer. The corresponding dependences for Mach–Zehnder modulators with different QW thicknesses are presented in Fig. 3. The modulator active part length L_m was taken to be 100 μm. The driving voltage was applied to one of the interferometer arms.

The plots in Fig. 2 demonstrate that the 12-nm-thick QW is characterised by the least driving voltage efficiency and the least optical loss (22 dB cm^{-1}) for the propagation of the fundamental waveguide TE mode. At the same time, 16-nm-thick QWs combine a high driving voltage efficiency and a wide range of linear change in the refractive index in dependence of the driving voltage. They exhibit a significant decay (30 dB cm^{-1}) at a wavelength of 1.55 μm, but nevertheless provide a phase difference of π for optical signals in different Mach–Zehnder modulator arms at a voltage of 1 V on the modulator active part length of 100 μm (Fig. 3). The 20-nm-thick QWs have even a higher driving voltage efficiency and provide a phase difference of π for optical signals at a voltage of 0.5 V and the same length of modulator active part. However, because of the strong decay (38 dB cm^{-1}), it is rather difficult to form passive elements of optical circuit with a minimum total loss.

3. Simulation of the element for light transfer into the waveguide

Let us consider in more detail the properties of optical waveguides based on multiple-QW InGaAlAs heterostructures (see Fig. 1). Figure 4 shows how the distribution of the fundamental optical mode field depends on the width of a waveguide based on QWs formed by an $In_{0.52}Al_{0.09}Ga_{0.38}As$/$In_{0.53}Al_{0.3}Ga_{0.17}As$ superlattice on an InP substrate (the driving voltage is zero). It can be seen that, with a gradual decrease in the waveguide width from 1.5 to 0.7 μm, the fundamental mode field is gradually pushed into the buffer layer of the two-layer rib waveguide. This mode has a large cross section (Figs 4b, 4c), a circumstance that significantly facilitates coupling of this waveguide with an optical fibre (having a microlens in the end part) and makes this process more efficient.

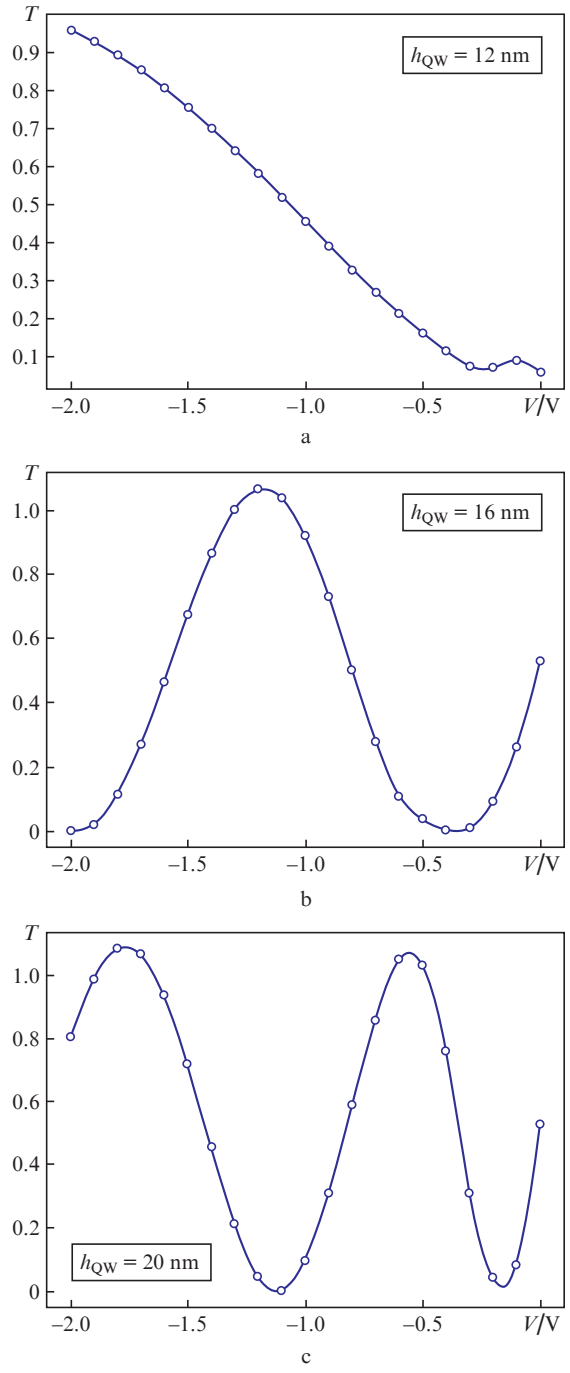

Figure 3. Dependences of the transmittance of optical-wave power through a Mach–Zehnder interferometer on the static electric voltage applied across the electrodes for QWs with thicknesses of (a) 12, (b) 16, and (c) 20 nm. The waveguide width is 1.5 μm, and the thickness of the waveguide layer containing 8 QWs is H_{QW} = 300 nm.

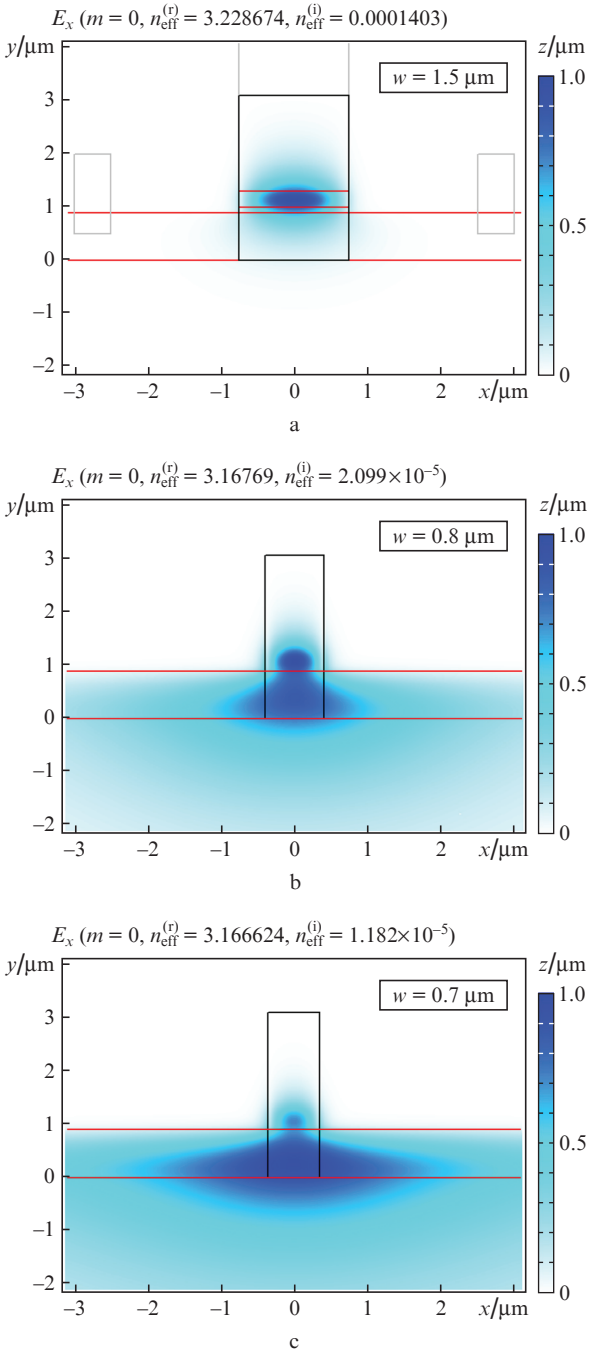

Figure 4. Transverse distribution of the electric field of fundamental TE mode in comb waveguides with widths of (a) 1.5, (b) 0.8, and (c) 0.7 μm. The structure consists of eight 16-nm-thick QWs.

A possible configuration of the coupling element using properties of a two-layer optical waveguide is shown in Fig. 5. It is intended for coupling the end with an optical fibre having a microlens, which provides a focal spot size of 3 μm. It is assumed that light is focused on the waveguide structure edge having an antireflection coating; therefore, Fresnel reflections were disregarded in the calculation.

This structure has a specific feature: a nonmonotonic change in optical waveguide properties with a change in the taper width. In particular, at thicknesses close to the operating waveguide width (1.5 μm), a change in the taper width causes a significant change in the ERI of the waveguide mode, but its energy is concentrated as previously in the QW region, and a high waveguide loss occurs. With a further decrease in the waveguide width, the ERI of the mode changes only slightly, but the mode spatial distribution undergoes a significant transformation (see Figs 4b, 4c) and the optical wave is characterised by low propagation loss. Therefore, to provide an efficient coupling, we applied an adiabatic taper with two different scales of variation in the width of the taper along its length (see Fig. 5). We used a taper profile in the form of two Gaussian functions with half-widths of $0.04L_T$ and $0.68L_T$ and amplitude coefficients of

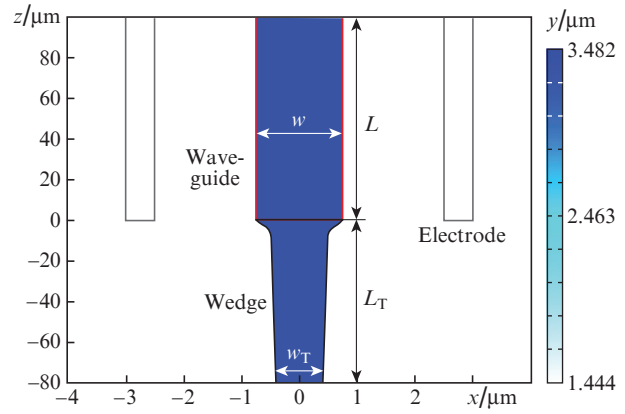

Figure 5. Element in the form of an adiabatic taper for the end-face coupling of optical fibre with a rib waveguide based on InAlGaAs QWs. A fibre having a lens in the end face is brought to the narrow part of the taper (below the figure). The waveguide width at the input and output of the adiabatic taper are, respectively, $w_T = 0.8$ μm and $w = 1.5$ μm and the taper length $L_T = 80$ μm; L is the electrode length.

$0.7(w - w_T)/2$ and $0.3(w - w_T)/2$, respectively, for the slow and fast change in the taper width. Here, w_T and w are, respectively, the waveguide widths at the input and output of the adiabatic taper of length L_T. The use of an adiabatic taper with a shape described by this function made it possible to reduce approximately by half the optical loss in the coupling element and shorten it by a factor of 3.

The principle of operation of the coupling element based on a double waveguide is illustrated in Figs 6 and 7. In particular, we calculated the efficiency of the edge-face input element for a rib waveguide formed by an $In_{0.52}Al_{0.09}Ga_{0.38}As/In_{0.53}Al_{0.3}Ga_{0.17}As$ superlattice on an InP substrate. Figure 6 shows the power loss for an optical wave with a wavelength λ, transmitted from the fibre output through the taper-shaped region to the output of the waveguide rectangular section of length L. The data for $L = 0$ show that the end-face loss introduced by the proposed element is ~1.5 dB. The calculations demonstrate a relatively high optical loss for the waveguides in multiple-QW structures based on the Stark effect; therefore, the total modulator length should not exceed 1 mm in order to reduce the introduced loss below 10 dB (~3 dB of which fall on the two coupling elements). Note that we disregard the additional optical loss due to the scattering by surface roughness in our calculations; this loss depends on the fabrication technology and generally equals ~0.3 dB mm^{-1}.

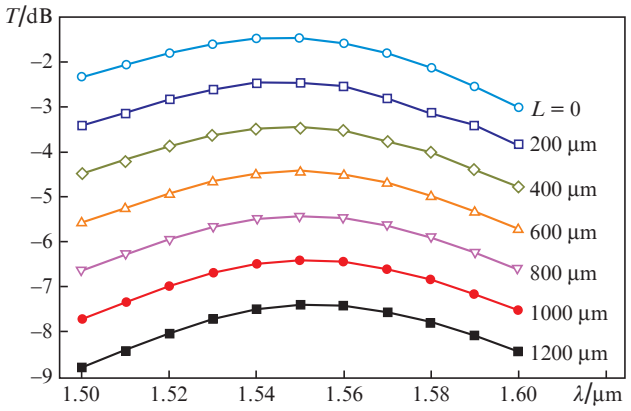

Figure 6. Spectral dependences of the optical-wave power transmission loss on the path from the fibre output to the end of the structure presented in Fig. 5 for optical waveguides of different lengths. The optical spot diameter at the focusing fibre output is 3 μm, $w_T = 0.8$ μm, $w = 1.5$ μm, and $L_T = 80$ μm. The structure consists of eight 16-nm-thick QWs.

The technological tolerances for fabrication of a taper-shaped coupling element with a waveguide are illustrated in Fig. 7 by the dependence of coupling efficiency (the wave power transmittance for a short waveguide with $L = 1$ μm) on the longitudinal fibre displacement at several tip widths. It can be seen that the coulpling efficiency per element remains relatively high (less than 2 dB per element) if the waveguide width is controlled with an error not larger than ±40 nm. The fibre position must be aligned to the waveguide boundary with an error of ~0.4 μm.

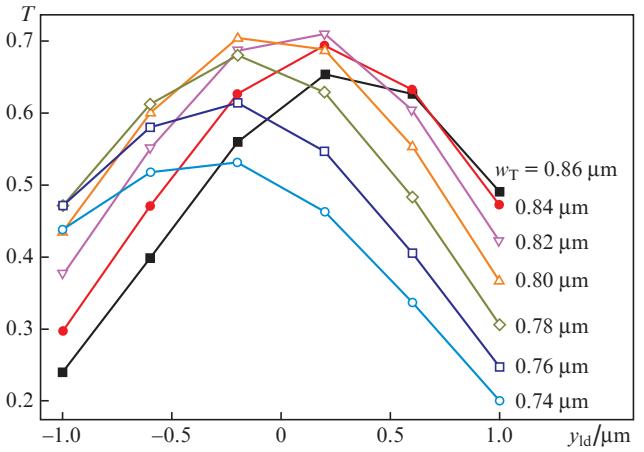

Figure 7. Transmittances of optical-wave power through the structure (Fig. 5) at different minimum tip widths w_T and longitudinal displacements y_{ld} of the focusing fibre; $w = 1.5$ μm, $L_T = 80$ μm, $L = 1$ μm, and $\lambda = 1.55$ μm. The structure consists of eight 16-nm-thick QWs.

4. Simulation of a Mach–Zehnder interferometer with MMI beam splitters 1×2 and 2×2

Researchers pay much interest to the optical modulator circuit in the form of a Mach–Zehnder interferometer with a beam splitter based on multimode interference (MMI). MMI-based devices were chosen for analysis as the most compact and technologically efficient. Here, use is made of a design with a beam splitter 1×2 at the modulator input and a beam splitter 2×2 at the modulator output (Fig. 8). In contrast to the standard case of two identical MMI beam splitters 1×2, this MMI combination has an interesting feature: due to built-in phase shift of π/2 for the combination of MMI beam splitters 1×2 and 2×2, the signal amplitude is identical at the two modulator outputs. Thus, the device is positioned at the working point, which does not need any additional shift in a wide range of optical wavelengths. The device is little sensitive to variations in external conditions (for example, temperature). In addition, there is a possibility of receiving and processing simultaneously two signals from two interferometer arms, and these signals have a much lower noise level in comparison with the standard geometry (1×2 and 2×1).

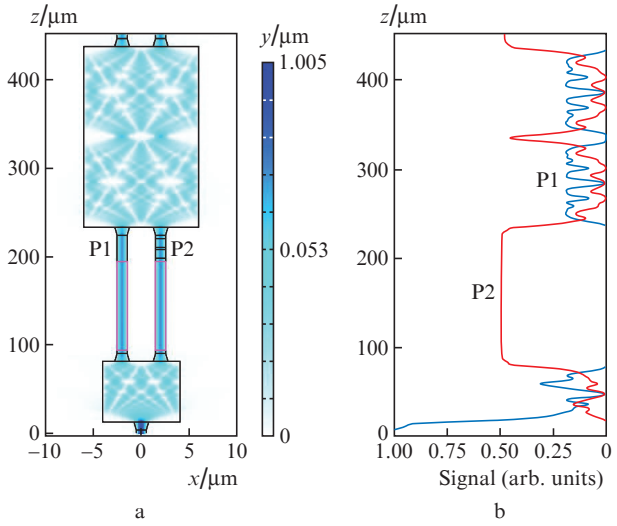

Figure 8. (Colour online) Mach–Zehnder interferometer with MMI beam splitters 1×2 and 2×2: (a) power distribution pattern for the left (P1) and right (P2) interferometer arms and (b) the wave field evolution during the wave propagation over the interferometer. Calculation by the 3D BPM method.

The results of 3D BPM numerical simulation show that the Mach–Zehnder interferometer with 1×2 and 2×2 beam splitters is relatively stable against fabrication errors and has low introduced loss (less than 0.6 dB) in the entire spectral range used for telecommunication systems (Fig. 9). For better visualisation, the results presented in Figs 8 and 9 correspond to the case where optical loss was disregarded. To calculate the total modulator loss, it is necessary to add the scattering loss at optical wave propagation (~0.3 dB mm^{-1}) and the loss in the modulator coupling with optical fibre (see Fig. 6). With allowance for all these factors, the total introduced loss of the proposed modulator should be less than 10 dB (9 dB for a 1-mm-long device at a wavelength of 1.55 μm, which is a sum of 2×1.5 dB (loss in the coupling with optical fibre), 0.6 dB (internal loss of Mach–Zehnder interferometer), 5 dB (additional propagation loss due to the quantum-confinement Stark effect), and 0.3 dB (waveguide loss because of the scattering from surface roughness).

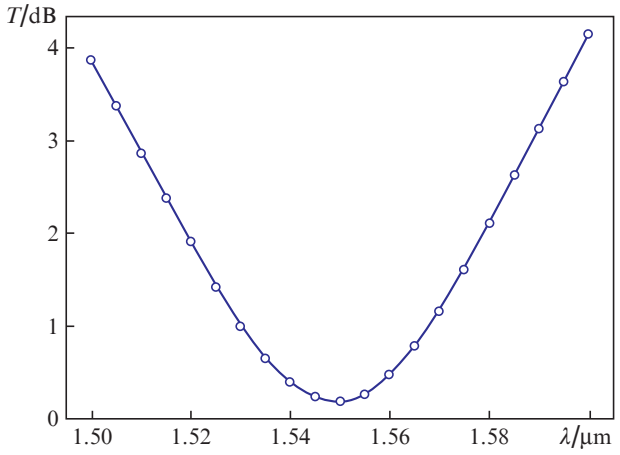

Figure 9. Spectral dependence of the total loss of Mach–Zehnder interferometer based on MMI splitters 1×2 and 2×2.

5. Simulation of the microwave properties of the modulator

The microwave properties of modulators based on the quantum-confinement Stark effect were simulated using the CST Microwave Studio Suite commercial software [17]. A preliminary simulation revealed that, at any reasonable sizes of InP-based modulator structure, one cannot match the modulator impedance with the 50-Ω external microwave circuit (this matching is necessary for minimising the reflection of microwaves and increasing the modulation efficiency). For this reason, we considered the push–pull circuit for microwave driving of modulator (Fig. 10), in which two modulator arms are connected in series (but operate in antiphase, in the push–pull mode). In this structure, electric current flows from one driving electrode to the other electrode connected in series through the waveguides located on an InP substrate with a high conductivity. Under these conditions, the impedances of the microwave channels of each waveguide arm are summed, thus facilitating matching of the impedance of entire coplanar line with the 50-Ω external microwave circuit. In addition, the electric field modulates in antiphase each arm of the optical Mach–Zehnder interferometer, which makes it possible to reduce by half the driving voltage at which a phase difference of π is obtained for optical signals in different interferometer arms.

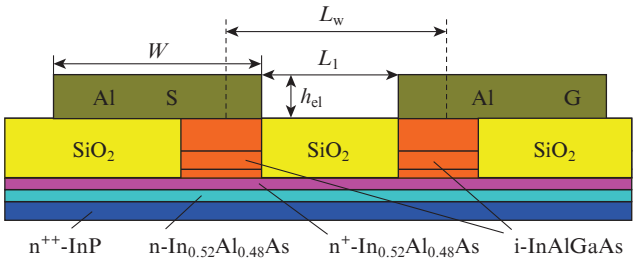

Figure 10. Schematic of the modulator operating in the push–pull mode with an electrode thickness h_{el} = 1.5 μm. The width of electrodes S and G is W = 8 μm, and the distance between the waveguide centres is L_w = 8 μm.

When simulating the structure, the sizes of modulator electrodes were varied to implement practically complete matching with the 50-Ω external microwave circuit at a frequency of 40 GHz and decrease the propagation loss of quasi-TEM-microwave mode in the coplanar waveguide structure. The distance L_w between the centres of two optical waveguides forming the Mach–Zehnder modulator arms was taken to be 8 μm. The width W of the electrodes to which a modulating electric signal is applied was 8 μm (Fig. 10). In this electrode geometry, the impedance of coplanar line is close to 50 Ω at a frequency of 40 GHz, due to which it can be matched with the 50-Ω external microwave circuit.

Changing the distance L_1 between the optical waveguides and the electrode width W, one can slightly vary the microwave decay, the microwave effective permittivity of free space (or effective refractive index), and the coplanar line impedance, which makes it possible to reduce the mismatch between the microwave and optical wave velocities in the waveguide and match the microwave channel with the 50-Ω external load.

The simulation included also calculation of the microwave electric field distribution in the transverse modulator

structure. Almost all the intensity of the vertical component of electric field is concentrated directly in the QW region of the optical waveguide, as a result of which conditions for efficient modulation of the refractive index in the QWs based on the quantum-confined Stark effect are provided. The horizontal component of electric field (along the QW boundary), being concentrated mainly in the gap between the waveguides, does not affect the modulator characteristics.

The numerical simulation showed that the proposed structure can be used to design microwave modulators based on the quantum-confined Stark effect on indium phosphide substrates. In particular, for the structure shown in Fig. 10, at a microwave frequency of 40 GHz, the line impedance is approximately 50 Ω, and the microwave loss is 3.8 dB at the modulator active part length L_m = 1 mm and a distance between the waveguide centres of 8 μm. Loss can be reduced to 2.8 dB by decreasing this distance to 4 μm; however, the wave impedance will decrease to 48 Ω in this case. A favourable factor is that the microwave effective refractive index (3.5) becomes close to the effective index of the fundamental optical mode (see Fig. 2a). This circumstance is very important for providing a wide modulation band [18], because one can match more exactly the microwave and optical wave velocities in the modulator.

6. Conclusions

We performed a numerical analysis of the electro-optic modulator with QWs based on $In_{0.52}Al_{0.09}Ga_{0.38}As/In_{0.53}Al_{0.3}Ga_{0.17}As$ superlattice on an InP substrate. These structures provide a highly efficient electro-optic control and form a double rib waveguide with unique optical properties. In particular, applying a smooth adiabatic change in the waveguide width, one can change several times the transverse size of the fundamental mode and thus provide a simpler and more efficient coupling between the waveguide and optical fibre. For example, for the minimum width of taper-shaped element, 0.8 μm, the coupling loss is 1.5 dB per element, which is an acceptable value for practical use in modulators based on the Stark effect. The optical and microwave properties of electro-optic modulator were described. The proposed modulator design with a total length less than 1 mm was shown to have total expected introduced loss (from fibre to fibre) of ∼10 dB in the telecommunication wavelength range.

Acknowledgements. We are grateful to Synopsys, Inc. [11] for supplying the licensed RSoft software for computer simulation of our structures. This work was supported in part by the Ministry of Science and Higher Education of the Russian Federation, unique project identifier RFMEFI58117X0026, in the part concerning the acquisition of software [11] and optimisation and development of the MMI calculation algorithm.

References

1. Green W.M.J., Rooks M.J., Sekaric L., Vlasov Y.A. *Opt. Express*, **15**, 17106 (2007).
2. Reed G.T., Mashanovich G., Gardes F.Y., Thomson D.J. *Nat. Photonics*, **4**, 518 (2010).
3. Wooten E.L., Kissa M.K., Yi-Yan A., Murphy E.J., Lafaw D.A., Hallemeier P.F., Maack D., Attanasio D.V., Fritz D.J., McBrien G.J., Bossi D.E. *IEEE J. Sel. Top. Quantum Electron.*, **6**, 69 (2000).
4. Sohler W., Hu H., Ricken R., Quiring V., Vannahme C., Herrmann H., Büchter D., Reza S., Grundkötter W., Orlov S., Suche H., Nouroozi R., Min Y. *Opt. Photonics News*, **19**, 24 (2008).
5. Liu J., Xu G., Liu F., Kityk I., Liua X., Zhena Z. *RSC Adv.*, **5**, 15784 (2015).
6. Tsarev A.V., Taziev R.M., Heller E., Chalony M. *Photonics Nanostruct. Fundam. Appl.*, **25**, 31 (2017).
7. Liu A., Liao L., Rubin D., Nguyen H., Ciftcioglu B., Chetrit Y., Izhaky N., Paniccia M. *Opt. Express*, **15**, 660 (2007).
8. Feng N.N., Liao S., Feng D.Z., Dong P., Zheng D., Liang H., Shafiiha R., Li G., Cunningham J.E., Krishnamoorthy A.V., Asghari M. *Opt. Express*, **18**, 7994 (2010).
9. Juodawlkis P.W., O'Donnell F.J., Bailey R.J., Plant J.J., Ray K.G., Oakley D.C., Napoleone A., Watts M.R., Betts G.E. *Proc. SPIE*, **5435**, 0277 (2004).
10. Mitchell P., Longone R., Janssen A., Garrett B., Luo J.K. *J. Optoelectr. Adv. Mater.*, **12**, 965 (2010).
11. RSoft by SYNOPSYS (https://www.synopsys.com/optical-solutions/rsoft.html), single license (2018).
12. Grote B., Heller E.K., Scarmozzino R., Hader J., Moloney J.V., Koch S.W., in *Advanced Simulation and Analysis of Optoelectronic Devices*. Ed. by J.Piprek (Springer, 2004).
13. Grote B., Heller E.K., Scarmozzino R., Hader J., Moloney J.V., Koch S.W. *Proc. SPIE*, **4986**, 413 (2003).
14. Piprek J. *Semiconductor Optoelectronic Devices* (San Diego: Academic Press, 2013).
15. Scarmozzino R., Gopinath A., Pregla R., Helfert S. *IEEE J. Sel. Top. Quantum Electron.*, **6**, 150 (2000).
16. Chow W.W., Koch S.W. *Semiconductor-Laser Fundamentals, Physics of the Gain Materials* (Berlin: Springer, 1999).
17. https://www.cst.com/products/cstmws, single license (2017).
18. Fuste J.A.I., Blanco M.C.S. *Opt. Lett.*, **38**, 1548 (2013).